Nanoscale

ROYAL SOCIETY
OF **CHEMISTRY**

PAPER
Anil Kumar Bandela, Udayabhaskararao Thumu *et al.*
Programmable precise kinetic control over crystal phase,
size, and equilibrium in spontaneous metathesis reaction for
Cs–Pb–Br nanostructure patterns at room temperature

NCNST

Check for updates

Programmable precise kinetic control over crystal phase, size, and equilibrium in spontaneous metathesis reaction for Cs−Pb−Br nanostructure patterns at room temperature†

Marek Piotrowski, [ID] ‡[a] Zhongsheng Ge, [ID] ‡[a] Yixi Wang, [ID] [a]
Anil Kumar Bandela [ID] *[b] and Udayabhaskararao Thumu [ID] *[a]

Growth kinetics involved in spontaneous random clustering of perovskite precursors to a particular cesium−lead−bromide (Cs−Pb−Br) nanocrystal (NC) is a poorly understood phenomenon and its spectroscopic investigation is highly challenging. There is scarcely any method that has been optimized yet in which perovskites and their related NCs of a particular size can be grown, viewed, or tuned to another by reaction handling. Here, for the first time, we shed light on the largely overlooked process of growth kinetics of these transformations throughout the reaction trajectory of anionic $[PbBr_x]^{n-}$ crystallization dictated by Cs^+ cation and report a simple and direct approach to control the metathesis reaction between two precursors (specifically Cs^+- and $PbBr_2$-associated oligomeric complexes) in one solvent at room temperature to monitor the NC growth characteristics in a stepwise manner even in the early stages of nucleation. Altering the molar ratio of the two precursors up to a factor of 10 leads to the formation of three prominent phases ($CsPbBr_3$, Cs_4PbBr_6, CsBr) as dictated by Cs^+ to trigger distinct morphological forms (nanobelts, nanoplatelets, rhombohedral NCs, pseudo-rhombic NCs, spherical CsBr NCs, cubic CsBr NCs) including a transient phase that is formed out of linearly self-assembled $CsPbBr_3$ clusters. Our results pave the way towards understanding spontaneous crystallization to develop well-defined, hassle-free routes for diverse perovskite NCs in a simple yet controlled manner.

Introduction

Spontaneous chemical reactions at room temperature (RT) yielding excellent materials of unique properties for a wide range of applications in electronics and optoelectronics are much sought and greatly regarded for the advancement of materials research. In view of easy device processing methods, reactions that do not require any external energy source are desirable to obtain well-controlled materials at the nanoscale by varying the stoichiometry of the precursors.[1] It is not conventional to employ such spontaneous reaction processes for controlling the shape, size, and crystal structures of noble metal nanoparticles and quantum dots.[2] In contrast to metal

and semiconductor nanosystems,[3] cesium lead halide perovskite nanocrystals (NCs) and their derivatives exhibit unique, spontaneous reaction tendencies.[4,5] Cesium lead halide perovskite NCs have a predominantly ionic lattice, so the reactions between oligomeric Cs^+, Pb^{2+}, and X^- precursors simply follow the metathesis route, *i.e.*, the redistribution of cations and anions in their respective complexes by the scission and regeneration of Cs–X and Pb–X bonds followed by the stabilization of the surface at the nanoscale by charged ligands (R–NH_3^+ and R–COO^-).[6,7] Recently, a few chemical equilibria have been suggested for the inter-phase transformations of $CsPb_2Br_5$, $CsPbBr_3$, and Cs_4PbBr_6 in the presence of external stimuli such as polarity, chelating agents, or thermal influence.[8–15] In addition, most of the systematic studies focused on thermodynamic control of these NCs at specific reaction conditions such as chemical nature of the ligand, temperature, use of a different source of halide, type of mixing, additives, *etc.*[16–23] Despite progress in thermodynamics, such as stable phase-controlled synthesis and structural transformations for shape- and size-controlled NCs, the growth kinetics mechanism for perovskite NCs is largely overlooked and is of increasing interest through systematic investi-

[a]Institute of Fundamental and Frontier Sciences, University of Electronic Science and Technology of China, Chengdu 610054, China. E-mail: uday@uestc.edu.cn
[b]Department of Chemistry, Ben Gurion University of the Negev Beer, Sheva 84105, Israel. E-mail: bandela@post.bgu.ac.il
†Electronic supplementary information (ESI) available: General information protocols of the titration conditions and 34 supplementary figures. See DOI: https://doi.org/10.1039/d2nr04102b
‡ M. P. and Z. G. contributed equally.

gation of reactions,[7] including robotic synthesis.[24] During a spontaneous reaction, a controlled equilibrium can be achieved to obtain targeted perovskite NCs,[25–29] for instance, nanoplatelets,[25,30] quantum dots,[26,31] nanobelts,[32–35] and nanosheets[36] *via* particular precursor ratios and selective ligands. However, it is anticipated that the best way to gain deep insight into kinetically stable intermediate states and their fine-tuning is to carefully study the reaction process at RT that could potentially nullify the dissipation of thermal energy, which otherwise could cause polar molecule byproducts, ligand destabilization, oriented self-assembly, phase transformations, *etc*. In this regard, herein, we demonstrate a systematic approach to understanding the direct influence of Cs^+ ion diffusion kinetics on the metathesis reaction that takes place among anionic $[PbBr_x]^{n-}$ and Cs^+ complexes towards the formation of perovskite NCs at RT in a non-polar solvent. In other words, this work aims not to study the products themselves or other variations in reaction conditions but rather to mainly focus on understanding the growth kinetics of these transformations throughout the reaction trajectory of anionic $[PbBr_x]^{n-}$ crystallization with Cs^+ cation. In a typical experiment, a microliter quantity (2–250 μL range) of precursor Cs-oleate ($\mathbf{P_{Cs\text{-}ol}}$) was titrated against a fixed $PbBr_2$ ($\mathbf{P_{Pb\text{-}br}}$) complexed with oleic acid (OA) and oleylamine (OLAM) in octadecene (ODE) in 2 mL hexane at RT in a 5 mL vial and shaken at 900 rpm (see a schematic illustration in Fig. 1 and ESI† for the detailed synthesis protocols). Because the conditions used in the original hot injection method are widely employed and still a primarily implemented strategy, the $\mathbf{P_{Cs\text{-}ol}}$ and $\mathbf{P_{Pb\text{-}br}}$ used in this protocol are the same as those in the original synthesis route.[4] In our approach, experiments were specially designed with a fixed volume of hexane as a solvent and tiny amounts of $\mathbf{P_{Cs\text{-}ol}}$ and $\mathbf{P_{Pb\text{-}br}}$ because such an approach not only provides the feasibility to vary the precursor stoichiometry ratios without abrupt changes in the concentrations but also provides a simple way to characterize the resultant NCs in solution without further dilutions or the necessity to conduct post-synthesis purification methods. At these reaction conditions, firstly, we investigated in detail the growth kinetics during titration of $\mathbf{P_{Cs\text{-}ol}}$ against $\mathbf{P_{Pb\text{-}br}}$; then, studies pertaining to concentration influence to produce kinetically favored crystal states; and finally, experiments that deal with the role of polarity in distorting the reaction memory.

Results and discussion

In this study, a solution of $\mathbf{P_{Cs\text{-}ol}}$ is directly titrated against $\mathbf{P_{Pb\text{-}br}}$, which is in stark contrast to the regular methods, and we observed that the initial milky white CsOA turned to a clear solution immediately after mixing both the precursors, and no sedimentation was found. In order to assess the reaction kinetics, initially, about 30 titrations were carried at infinitesimally small (1 μL) increments of $\mathbf{P_{Cs\text{-}ol}}$, specifically 2, 3, 4, 5, ..., 30 μL. In these regions, the spectral changes are very sensitive to the amounts of $\mathbf{P_{Cs\text{-}ol}}$ whereas changes are less sensitive to further addition. Therefore, subsequent titrations are performed at each 10 μL increment of $\mathbf{P_{Cs\text{-}ol}}$ from 40 to 250 μL. The $\mathbf{P_{Pb\text{-}br}}$ reacts with $\mathbf{P_{Cs\text{-}ol}}$ during titration and keeps on proliferating from one phase to another. Thus, overall, around 50 titrations and their repetitions at various reaction times were performed. Each sample was carefully studied by spectroscopy and microscopy analysis and a conclusion was arrived at to divide these precursor ratios into three categories: $\delta_1 = 1:0.03$ to $1:1$, $\delta_2 = 1:1$ to $1:5$, and $\delta_3 = 1:6$ to $1:10$ (S2-Table 1†), where δ = mole ratio precursors ($\mathbf{P_{Pb\text{-}br}}/\mathbf{P_{Cs\text{-}ol}}$). The colorless precursor solutions turned to yellowish or pale green in the δ_1 region, and the solutions turned to colorless with further incremental additions of $\mathbf{P_{Cs\text{-}ol}}$ in δ_2 and δ_3 regions (Fig. 1a and Fig. S1†). Optical absorption spectra of the NCs at δ_1, δ_2, and δ_3 exhibit characteristic absorption peaks at 420 nm and 313 nm, corresponding to two monolayers of $CsPbBr_3$[24] and Cs_4PbBr_6,[37,38] respectively, whereas a featureless spectrum at δ_3 corresponds to CsBr NCs (Fig. 1b). In between δ_1 and δ_2, there is another product not related to any of these crystal phases whose absorption is around 370 nm attributed to transient phase (TP) of linear assemblies of $CsPbBr_3$ clusters between $CsPbBr_3$ and Cs_4PbBr_6. Fig. 1c is a schematic illustration of the formation of three prominent phases ($CsPbBr_3$, Cs_4PbBr_6, and CsBr) as dictated by Cs^+ to trigger distinct morphologies (nanobelts, nanoplatelets, rhombohedral NCs, pseudo-rhombic NCs, spherical CsBr NCs, cubic CsBr NCs). The next section deals with the in-depth study of these systematic absorption changes with respect to the minor changes of $\mathbf{P_{Cs\text{-}ol}}$ against $\mathbf{P_{Pb\text{-}br}}$. The ratios ($\delta$) and the resulting crystal phase, shape, and sizes are detailed in ESI (S2-Table 1†).

The structural conformation of the samples was studied by analyzing powder X-ray diffraction (XRD) patterns of the
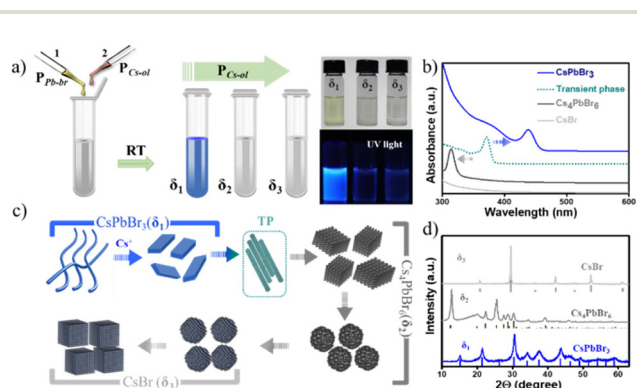

Fig. 1 Schematic illustration of the RT synthesis of Cs−(Pb)−Br nanostructures at different amounts of $\mathbf{P_{Cs\text{-}ol}}$ titrated against $\mathbf{P_{Pb\text{-}br}}$ (the amount of $\mathbf{P_{Cs\text{-}ol}}$ increased from 2 μL to 250 μL, δ_1 to δ_3) in hexane (a) and absorption spectra (b) of solutions collected from reaction vials corresponding to four main regions (δ_1–δ_3) with three types of crystal phases and a transient phase. (c) Schematic representation of Cs^+-concentration-triggered growth of three prominent phases and their distinct morphologies – nanobelts, nanoplatelets, rhombohedral NCs, pseudo-rhombic NCs, spherical CsBr NCs, cubic CsBr NCs including a transient phase. (d) Powder X-ray diffraction patterns of three selected samples in the three regions of δ_1, δ_2, and δ_3. The vertical bars indicate the ICSD reference patterns of $CsPbBr_3$, Cs_4PbBr_6, and CsBr NCs.

selected samples in the three regions (Fig. 1d), where all peak positions observed represent $CsPbBr_3$, Cs_4PbBr_6, and CsBr crystal phases. Also, mixed phases are observed in the regions where the borders of one phase to another phase are overlapped (Fig. S2†). The stoichiometry ratios of the pristine nanostructures were further confirmed by HAADF-STEM EDS analysis of pure and mixed regions. The atomic percentages values of Cs : Pb : Br of 1 : 1 : 2.6, 4 : 1 : 5 and 1 : 0.06 : 1.1 are in good agreement with those of the three phases $CsPbBr_3$, Cs_4PbBr_6, and CsBr, respectively (Fig. S3 and S4†).

Some of the representative spectra are compared to follow the absorption changes in a stepwise manner that clearly showcase the phase transformations going from δ_1 to δ_3 regions (Fig. 2a). In δ_1, initially an addition of 2 μL of $\mathbf{P_{Cs\text{-}ol}}$ against $\mathbf{P_{Pb\text{-}br}}$ evoked a rapid spectral change with the appearance of an absorption band at 390 nm, which red shifts to 420 nm over time in a span of 15 min (Fig. S5†). These two bands correspond to single- and two-monolayered $CsPbBr_3$ nanostructures, respectively.[24,36] Later on, the changes were slowed down, indicating the formation of a fairly stable phase of $CsPbBr_3$ NBs. Thus, the major changes are (i) appearance of a new absorption band at 390 nm, (ii) appearance of a shoulder at *ca.* 420 nm, (iii) rise of the shoulder to a strong

Fig. 2 (a) Absorption spectra of the transformation of Cs–(Pb)–Br nanostructures from $CsPbBr_3$ to Cs_4PbBr_6 NCs to CsBr NCs *via* the intermediate transient phase. The systematic trend of characteristic peak positions is labelled with different colours to represent the four major bands at ≈430 nm, 420 nm, 370 nm, and 313 nm. The upper black trace is featureless, corresponding to CsBr NCs. The top arrow indicates the incremental addition of $\mathbf{P_{Cs\text{-}ol}}$ to the reaction. Titrations were carried out at RT and a constant concentration of the host, $\mathbf{P_{Pb\text{-}br}}$. (b) The appearance of characteristic absorption bands (≈430 nm, purple; 400 nm, blue; 370 nm, red; 317 nm, black) and their gradual progress during the titration of $\mathbf{P_{Cs\text{-}ol}}$ from 2 μL to 200 μL. (c) STEM image of the intermediate product formed between $CsPbBr_3$ and Cs_4PbBr_6 phases corresponding to the absorption at 370 nm, which persisted for a long titration period from 20 to 50 μL of $\mathbf{P_{Cs\text{-}ol}}$ addition (red trace in b). (d) The changes in PL intensity and the PL wavelength with respect to the titrations of (b).

absorption band at 420 nm at the expense of decreasing absorption at 390 nm (that is, the transformation of single- to two-monolayered $CsPbBr_3$ nanostructures). Remarkably, the spectral changes are accompanied by the appearance of isosbestic points at 408 and 380 nm (Fig. S5†), indicating a stoichiometric conversion of single-layer (390 nm) to two-monolayered nanostructures (420 nm). These isosbestic points are clearly seen with an increase in the Cs^+ amount until the titrations of 12 μL of $\mathbf{P_{Cs\text{-}ol}}$ to $\mathbf{P_{Pb\text{-}br}}$. A few more increments later, the isosbestic features are distorted and finally vanished beyond certain additions of $\mathbf{P_{Cs\text{-}ol}}$. The presence of distorted isosbestic features is due to the two simultaneous growth and shrinkage transformations which significantly lead to blue as well as red shifts in the absorption spectra with the increase in the presence of $\mathbf{P_{Cs\text{-}ol}}$ (Fig. S6–S9†). In Fig. 2a (in the δ_1 region), the absorption was collected after 4 hours of reaction, showing the band at 430 nm.

Interestingly, overall, this band at 430 nm undergoes a gradual blue shift (Fig. 2a, Fig. S6–S8†) during incremental addition of $\mathbf{P_{Cs\text{-}ol}}$ from 2 to 20 μL. The spectrum gradually loses its original absorption structure with a blue shift from 430 nm to 400 nm and then to an entirely new spectrum with absorption at 370 nm (Fig. 2a and Fig. S9†). Afterwards, an era of new region δ_2 begins with the emergence of zero-dimensional Cs_4PbBr_6 NCs as a dominating product with a clear characteristic absorption band at 313 nm (Fig. 2a and Fig. S10†). This crystal phase remained from the titration of 50 μL to 120 μL of $\mathbf{P_{Cs\text{-}ol}}$ against $\mathbf{P_{Pb\text{-}br}}$. Similar to the above-mentioned δ_1 condition, a rapid reaction change in the absorption fine structure (Fig. S11†), that is, the appearance of a broad peak composed of the absorption at 313 nm and 320 nm from Cs_4PbBr_6 and $[PbBr_4]^{2-}$, respectively, was seen immediately after mixing the precursors at δ_2 (Fig. S10,† 100 μL to 180 μL of $\mathbf{P_{Cs\text{-}ol}}$). Beyond these, a new region δ_3 occurred where the absorption is nearly featureless, corresponding to CsBr NCs (Fig. 2a, black trace; and Fig. S12†). As one might have expected, no further changes in the absorption spectra were observed when $\delta_3 = 1 : 20$ equivalent of $\mathbf{P_{Cs\text{-}ol}}$ was added.

Fig. 2b unambiguously indicates the appearance of four prominent absorption bands during the course of titration of $\mathbf{P_{Cs\text{-}ol}}$ from 2 to 200 μL. It is evident from the data that the characteristic $CsPbBr_3$ nanostructure absorption at 435 nm could occur only at the lower Cs^+ additions (2 to 11 μL); later, it undergoes a clear shift from 435 nm to 420 nm from around 12 μL addition of $\mathbf{P_{Cs\text{-}ol}}$. This absorption band further blue shifts to 370 nm with a small band at 400 nm for the subsequent incremental additions of $\mathbf{P_{Cs\text{-}ol}}$ (also refer to Fig. S13†). The blue shift of the $CsPbBr_3$ absorption peaks with an increased amount of Cs^+ is clearly indicative of the size reduction in the nanostructure. The emergence of the absorption peak at 370 nm with a shoulder peak at 320 nm is not so clearly observed or identified in Cs–Pb–Br literature to date, even for single-monolayer sizes. The absorption band of one-monolayer 2D $(OLAM)_2PbBr_4$ sheet is at 398 nm, as seen in the literature.[36] We ruled out the other possible compositions to characterize this intermediate phase such as
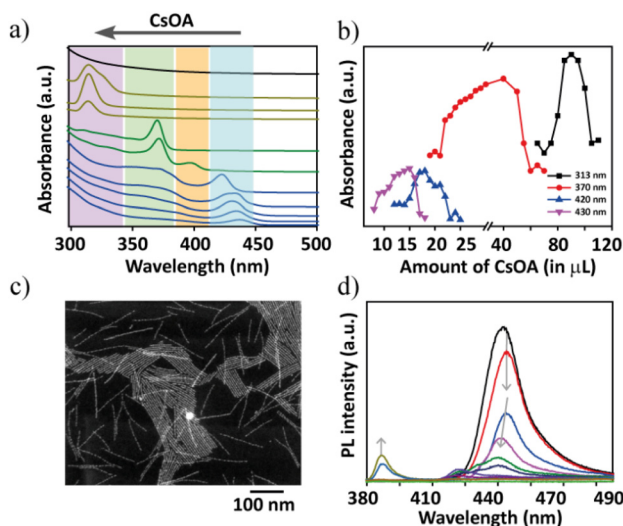
$CsPb_2Br_5$ and $PbBr_2$ NCs in the reaction medium because their absorption peaks are supposed to be around 320 to 350 nm, respectively.[24] In our studies, we observed that this absorption band was relatively stable without any sign of degradation for about 24 hours (Fig. S9†) and also persistent for a more extended titration volume from 26 μL to 70 μL of P_{Cs-ol} against P_{Pb-br} signifying it is a long-standing transient state. In view of their emission (see the next section), we attributed this phase to being made up of $CsPbBr_3$ clusters. In TEM, defined structures related to this transient state are composed of a linear arrangement of $CsPbBr_3$ clusters into ultra-thin structures (Fig. S14†). However, the HADDF-STEM image shows the presence of ultra-thin nanoplatelets (NPs) of bright contrast (Fig. 2c and Fig. S15†) and the morphology suggests linear assembled structures. In a set of reports, it was shown that nanoclusters[39] and particles[40] could assemble in a one-dimensional fashion under the impact of electrostatic interactions. Thus, it is possible that these NPs are intermediate state structures, and we attribute these structures to $CsPbBr_3$ clusters that assembled into ultra-thin NBs. However, more detailed studies are required to understand the origin of the optical properties of this structure. From 70 μL to 120 μL, the Cs_4PbBr_6 NC phase dominates with a maximum yield at 90 μL addition of P_{Cs-ol}. Beyond 120 μL to 200 μL, the reactions show a weak absorption at 313 nm and 320 nm. These peaks are inextricably linked to $[PbBr_6]^{4-}$ and the peak intensities are interchangeable over time. This scenario implies that these Cs_4PbBr_6 NCs and $[PbBr_6]^{4-}$ are in chemical equilibria.[41]

Photoluminescence (PL) studies of these reactions further confirm the blue shift in the emission with incremental Cs^+ additions. In addition to the blue shift, the emission intensity drastically reduced for the single-layer species reminiscent of nanoplatelets, and such poor emission properties are attributed to the increased surface defects at this atomic scale of perovskites. At 30 μL of (P_{Cs-ol}) a new and weak emission at 380 nm appeared corresponding to the intermediate transient species (λ_{abs} of 370 nm). The results of PL experiments indicate that the influence of stoichiometry on the shape and crystal structure transformations results in the change of NC emission properties. Fig. 2d shows the PL results with an increase in the concentration of Cs^+ ions. At molar ratios $\delta = 1:0.25 - \delta = 1:1$, nanobelts emit cyan blue at 420 nm. In the following stages, Cs^+ increase results in the appearance of a very weak emission at 400 nm corresponding to one-monolayer-thick nanosheets, and, next, the appearance of a weak emission at 380 nm. As expected for other phases Cs_4PbBr_6 and $CsBr$, we have not observed any luminescent features in all NC systems at values $\delta \leq 1$ (Fig. 2d).

The TEM measurements of the spontaneous reaction solution at the lower δ_1 region show formation of atomically thin lamellar nanoplatelets (NPs), which correlate to the one-monolayer thickness (Fig. S16†). These structures subsequently arrange into two-monolayer perovskite structures within several minutes and further grow to nanobelts of length 1–3 μm and width ~6 nm (Fig. 3a). At moderate δ_1, shortening and thinning of NBs take place, resulting in NPs of 20–30 nm
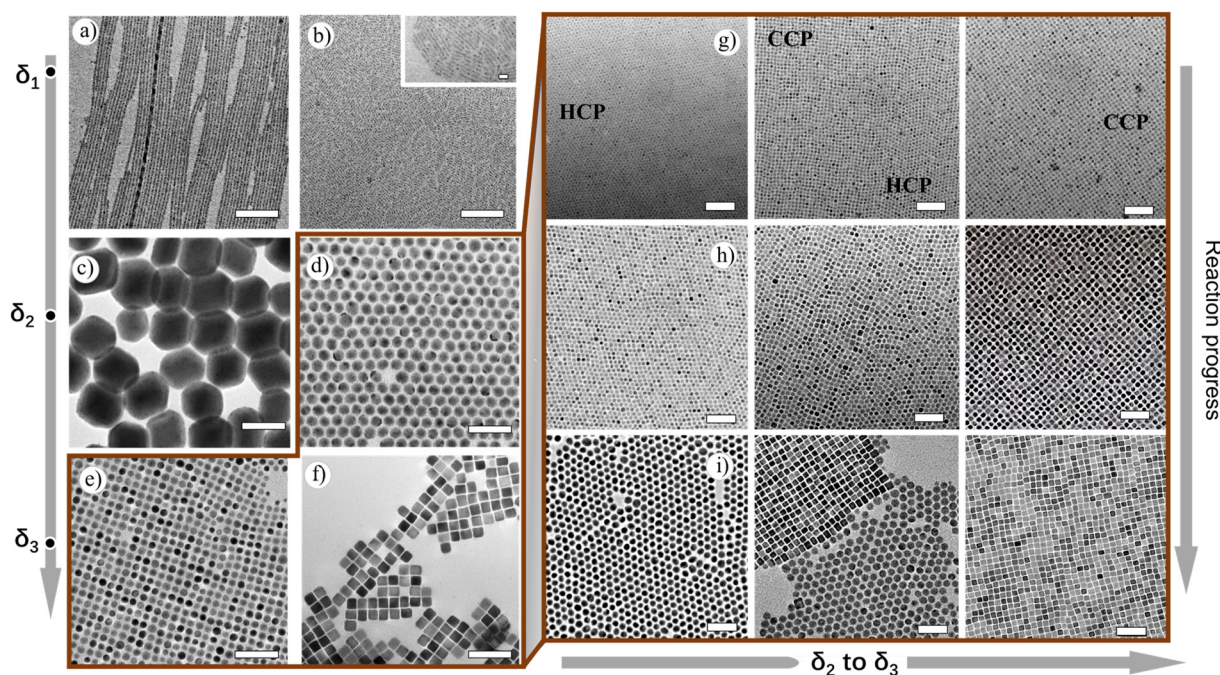

Fig. 3 TEM images collected at reaction condition δ_1, corresponding to $CsPbBr_3$ NBs (a) and nanoplatelets (b). (c and d) TEM images collected for reaction condition δ_2, related to two different sized Cs_4PbBr_6 structures. (e and f) TEM images collected for reaction condition δ_3, related to spherical and cube-shaped $CsBr$ NC structures. (g, h and i) TEM images of the NCs with two different packings (HCP and CCP) during the reaction progress while transferring reaction conditions from δ_2 to δ_3. Scale bars are 100 nm in all the regular images and 10 nm for the image in the inset of (b).

in length and ∼3 nm in width (Fig. 3b, inset). At the lower δ_2 region, a different behavior has been observed for Cs-rich conditions, where the surface plane is mainly ended with Cs$^+$ ions. At this ratio, we started to observe the appearance of additional phases in the solution along with CsPbBr$_3$ NPs, and they are ∼100 nm-sized rhombohedral Cs$_4$PbBr$_6$ NCs (Fig. S17†). At this stage, the absorption spectra showed the presence of mixed peaks centered at 400 nm (weak), 370 nm, and 313 nm as well. At moderate δ_2 values, NPs disappear while 100–150 nm-sized Cs$_4$PbBr$_6$ rhombohedral NCs are exclusively seen (Fig. 3c). On further increase in δ_2, the size of the rhombohedral Cs$_4$PbBr$_6$ NCs decreases, and apparently ∼20 nm spherical Cs$_4$PbBr$_6$ NCs have emerged (Fig. 3d). Remarkably, these are highly monodisperse, and they form large self-assembled monolayers of hexagonally packed sheets upon drop-casting of the as-made sample in hexane on a TEM grid (Fig. S18†).

Now one important question arises: What happens if the Pb^{2+} ratio further reduces in our reaction conditions? Intending to answer this question, we decided to further increase the amount of Cs$^+$, which eventually decreases the Pb^{2+} availability for the reaction. At lower δ_3, a mixed phase consisting of spherical particles (≈12 nm) with two types of packing tendencies has been observed (Fig. S19 and S20†). Even though all NCs formed are spherical, they are arranged in three different packings through self-assembly upon solvent evaporation. The three different packings are CCP, HCP, and mixed quasi-crystalline packing, which implies the presence of two types of NC structures (Fig. 4 and 5a–c). The XRD data confirm the presence of both Cs$_4$PbBr$_6$ and CsBr NCs (Fig. 5d). The results of HRTEM studies in Fig. 4 are in agreement with the assigned crystal phase compositions. The lattice spacings of 0.68 nm, 0.4 nm, and 0.33 nm correspond to (100), (110), and (131) of the Cs$_4$PbBr$_6$ phase, respectively. The lattice spacings of 0.43 nm and 0.3 nm correspond to (100) and (110) of
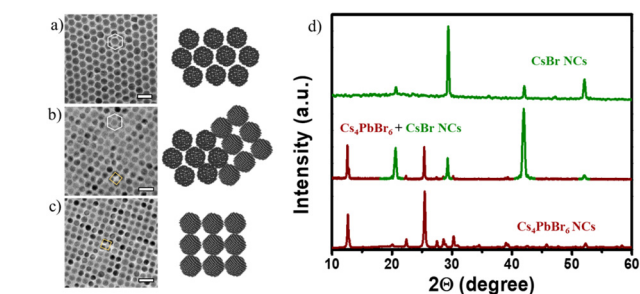

Fig. 5 (a–c) TEM images of NCs with two different packings (hexagonal close packing, HCP, and cubic close packing, CCP) while the reaction condition was transferring from δ_2 to δ_3. Scale bars are 20 nm in all the images. (d) Powder XRD patterns of the samples in the regions of δ_2 and δ_3 corresponding to Cs$_4$PbBr$_6$ and CsBr NCs along with their mixed region.

the CsBr phase, respectively. Typically, the single perovskite NCs assemblies lead to a simple cubic packing following the cube-shaped morphology. In addition, Kovalenko *et al.* explored other complex factors such as shape and steric influences for designing functional materials formed *via* this NC self-assembly.[42] We propose that the presence of the unique packing pattern of CsBr and Cs$_4$PbBr$_6$ could result from different ligand structures around the spherical NCs. This kind of dynamic change in the arrangement has also been observed in soft-matter materials, such as polymers. Recently, Pradhan *et al.* found such packing differences in pseudo-spherical CsPbBr$_3$ NCs due to the change in their facets.[19,43] Such unique self-assembly arrangements are seen even from the initial stages, since the reaction process is also consistently rapid even at δ_2 and δ_3 conditions as confirmed in TEM, with the formation of tiny spherical Cs$_4$PbBr$_6$ (≈6 nm) and CsBr NCs (≈3 nm) (Fig. 3g–i and Fig. S21–S24†). Even though both the NCs are spherical, their arrangement is unique, *i.e.*, HCP
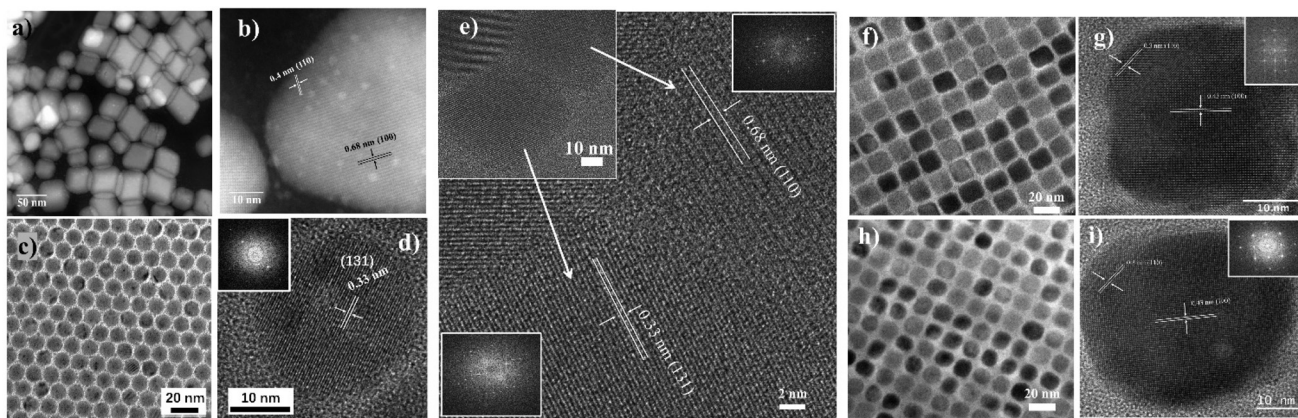

Fig. 4 (a and b) HAADF-STEM image of the 100 nm Cs$_4$PbBr$_6$ NCs prepared at the lower δ_2 region. (c and d) TEM images of the ≈15 nm Cs$_4$PbBr$_6$ NCs as self-assembled monolayers prepared at higher δ_2 regions. (e) TEM image of isolated Cs$_4$PbBr$_6$ NCs and their HRTEM analysis. TEM images of cubic (f) and spherical (h) CsBr NCs and their respective HRTEM images (g and i). The lattice spacings of 0.68 nm, 0.4 nm, and 0.33 nm correspond to (100), (110), and (131) of the Cs$_4$PbBr$_6$ phase, respectively. The lattice spacings of 0.43 nm and 0.3 correspond to (100) and (110) of the CsBr phase, respectively.

for Cs$_4$PbBr$_6$ and CCP for CsBr seeds (Fig. 3g). At moderate δ_3, the spherical CsBr NCs ($\approx$15 nm) were the dominating fraction and arranged in CCP fashion (Fig. 3e–h). At higher δ_3 = 1 : 8 to 1 : 10, with a further increase of the Cs$^+$ precursor amount in the reaction, the tendency to form cube-shaped CsBr ($\approx$20 nm) is completely dominant (Fig. 3f–i). It is worth noting that the residual amount of Pb^{2+} could not suppress the formation of Pb^{2+}-free CsBr structures. This observation is justifiable based on two reasons: (i) the relative reduction of Pb^{2+} in comparison to other ions (Cs$^+$ and Br$^-$); (ii) an increase in the amount of OA in solution could bind Pb^{2+} and is not involved in the reaction. Increasing the amount of **P$_{Cs-ol}$** adds both Cs$^+$ as well as OA into the reaction medium; however, the amount of OA is very little (1 μL **P$_{Cs-ol}$** contains 0.0625 μL of OA; overall 2.5 μL OA in 40 mL octadecane in a typical synthesis; details in ESI†) which did not alter the reaction products as confirmed through the experiments maintaining at constant OA (Fig. S25†). The absorption profiles show the same trend in the presence and absence of small additions of OA along with **P$_{Cs-ol}$**, reflecting the similar characteristic crystal phase irrespective of minute changes in the OA amounts. Consequently, these minute changes in ligand concentrations alter the morphology of a particular phase as discussed below.

At the same condition, soft-edged cube-shaped CsBr NCs were formed upon the addition of small (1–3 μL) quantities of OA. Typically, OA supports the formation of sharp edges of NCs, whereas OLAM suppresses the sharp edges leading to spherical NCs (Fig. S26 and S27†). Further increase in the Cs$^+$ ions in δ_3 (1 : 10) lowers the Pb^{2+} amounts to result in the formation of sharp-edged highly monodisperse CsBr nanocubes readily undergoing square packed assembly on TEM grids into 200 nm to 1 μm square-shaped sheets (Fig. S28†). Beyond this δ (1 : 10) value, formation of larger and polydisperse CsBr nanocubes has been observed (Fig. S29†). Overall, in these δ_1 to δ_3 regions, we demonstrated that size, shape, structure, and surface anisotropy could be kinetically controlled solely based on the amount of Cs$^+$ ions. Moreover, we believe such dynamic changes in the packing patterns, hexagonal close packing or face-centered cubic packing, based on the type of morphology, size, and crystal structure of NCs even from their nucleation stages, provide simple traditional microscopic crystal structure and uniqueness from others of the same size.

Another important issue is dealing with the chemical equilibria which could be reversible to either side of the reaction providing requisite chemical inputs. To crosscheck our hypothesis, first, CsPbBr$_3$ NBs were created by subjecting the titration reaction at δ_1 conditions whose characteristic absorption peak at 430 nm is shown in Fig. 6a. These pre-preformed NBs were subjected to post-modification through forward titration reaction by adding the required amount of **P$_{Cs-ol}$**. Here, the forward titration reaction indicates that first the NBs are formed at δ_1 conditions, and next the reaction conditions are shifted to δ_2 by providing additional δ_1. During this process, the absorption peak shows a clear blue shift from 430 nm to 313 nm (Fig. 6a), the TEM images corresponding to the obvious structural and morphology changes from CsPbBr$_3$ to Cs$_4$PbBr$_6$ (Fig. 6b). After
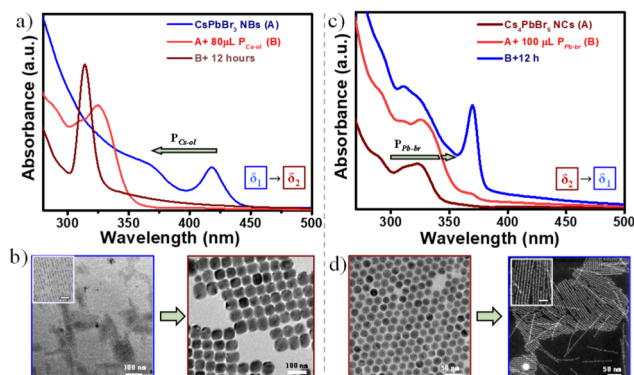

Fig. 6 (a) Absorption spectral studies of reaction, with the deliberate shifting of reaction conditions *via* introducing additional **P$_{Cs-ol}$** to the already prepared CsPbBr$_3$ NBs at δ_1 condition. Initially, NB structures are made by titrating 5 μL of **P$_{Cs-ol}$** with 100 μL of **P$_{Pb-br}$** in 2 mL hexane (A), its characteristic absorption spectrum of 430 nm being represented by a blue trace. At this point, 80 μL **P$_{Cs-ol}$** was added (B) in order to shift the reaction toward the formation of Cs$_4$PbBr$_6$ NCs, confirmed by the peak at 313 nm (brown trace) upon 12 h of reaction. (c) Absorption spectral studies of reaction, with deliberate reversing of the reaction conditions *via* introducing additional **P$_{Pb-br}$** to the already stabilized Cs$_4$PbBr$_6$ NC system. Initially, Cs$_4$PbBr$_6$ NC structures are made at δ_2 conditions by titrating 80 μL of **P$_{Cs-ol}$** with 100 μL of **P$_{Pb-br}$** in 2 mL hexane (A), the characteristic absorption peak being at 313 nm (brown trace). At this point, 100 μL **P$_{Pb-br}$** was added (B) in order to shift the reaction backward to the formation of CsPbBr$_3$ clustered NWs, confirmed by the peak at 370 nm upon 12 h of reaction. (b–d) TEM and STEM images representing the morphology changes during the forward and backward titration reactions. Scale bars of the insets are 20 nm.

12 hours of reaction time, there are pure Cs$_4$PbBr$_6$ NCs, and such are the conditions originally seen at initial δ_2 condition. In another case, at first, the Cs$_4$PbBr$_6$ NCs mixed with [PbBr$_6$]$^{4-}$ were created by titrating at δ_2 conditions. This reaction was subjected to backward titration conditions by adding the required amount of **P$_{Pb-br}$** leading to the appearance of a new absorption peak at 370 nm (Fig. 6c). TEM images show the transformation of spherical Cs$_4$PbBr$_6$ NCs to CsPbBr$_3$ clustered NBs (Fig. 5d), such conditions being originally seen at higher δ_1. Such reversible equilibrium is not successful in the case of δ_2 to δ_3. This could explain the influence of chemical equilibrium on the size and morphology of the NCs (discussed in the next section).

The crystalline products at different δ_1, δ_2, and δ_3 conditions can be explained in the following way. The sources of Pb^{2+} and Br$^-$ ions are apparently from PbBr$_2$, so a fixed amount of **P$_{Pb-br}$** results in the equivalent amount of Pb^{2+} and doubles the amount of Br$^-$ concerning incremental addition of Cs$^+$. The δ_1 region conditions are similar to a typical synthesis of CsPbBr$_3$ NCs in terms of precursor ratio where the amount of Pb^{2+} used for the synthesis is higher than that of Cs$^+$ in the reaction; hence Pb-oleate and PbBr-oleate are the expected byproducts. In the case of the lower Cs$^+$ addition side of δ_1, we observed the formation of NBs, and higher Cs$^+$ addition leads to nanoplatelets. The CsPbBr$_3$ NB formation can be explained by the cooperative effect of stoichiometry,

and micelle-based linearly assembled Pb$^+$, Br$^-$ complexed OA, and OLAM ligand interactions; the first one dictates CsPbBr$_3$ (Fig. 7a), and the latter directs the NB morphology. With a further increase of the Cs$^+$ amount, the competitive force between the interconnection among [PbBr$_6$]$^{4-}$ octahedra *versus* Cs$^+$ separated octahedra. In this situation, the NBs become shortened and turn to NPs as seen in TEM images and blue shift in the absorption. When the incremental addition of Cs$^+$ reaches δ_2, the second factor dominates that pushes the crystallization toward the crystal structure where octahedra are separated by Cs$^+$ ions for the formation of Cs$_4$PbBr$_6$ (Fig. 7b). At this condition, instead of preferring the three-dimensional growth while maintaining the CsPbBr$_3$ phase, a phase transformation occurs and results in the formation of Cs$_4$PbBr$_6$ NCs. Interestingly, beyond the $\delta = 1:6$ region, the transformation to CsBr NCs indicates that the residual Pb^{2+} is not enough to participate in the reaction; hence it could no longer influence the reaction. However, in the presence of an excess amount of Cs$^+$, cesium rapidly reacts with bromine (double the concentration of Pb^{2+}), causing the nucleation of CsBr NCs (Fig. 7c). Importantly, the concentration of Cs$^+$ ions creates competitive forces which alter the growth kinetics determining the size and shape of particular NCs (NBs *vs.* NPs; 100 nm *vs.* 20 nm Cs$_4$PbBr$_6$ NCs; or spherical *vs.* cubic CsBr NCs). Few assumptions are expected for the cause of the size variation in these NCs. As shown in earlier sections, there is a dynamic equilibrium among CsPbBr$_3$ and Cs$_4$PbBr$_6$ systems. At increased Cs$^+$ concentrations, CsPbBr$_3$ NB equilibrium shifts to Cs$_4$PbBr$_6$ NCs, limiting the dissolution of the resulting crystal phase and resulting in the larger sizes of Cs$_4$PbBr$_6$ NCs. Whereas the tendency of balanced equilibrium among Cs$_4$PbBr$_6$ and CsBr systems in the middle of δ_2 and δ_3 regions prefers competition among the crystal phases at rapid formation, more dissolution results in smaller NCs. Finally, at

the higher δ_3 region (dominated by Cs$^+$ concentrations, the solubility of Pb^{2+} in the presence of OA), equilibrium shifts toward the formation of CsBr NCs and results in larger CsBr NCs. However, for an in-depth understanding of mechanistic insights, further qualitative studies are required on this system.

To better understand the kinetic control over the crystallization process, as a proof of concept, we studied the impact of dilution at δ_1 as this region exhibits visible changes (Fig. 7d). At $\delta_1 = 1:0.25$, the prerequisite amounts of **P$_{Cs-ol}$** to the host **P$_{Pb-br}$** at initial concentration lead to ultrathin NB formation. PL emission spectra of these NBs were collected at two different constant concentrations during the reaction progress over 24 hours (refer to ESI for experimental details†). The rising blue lines in Fig. 7e indicate original solutions during reaction progress at 1 h, 2 h, 3 h, 6 h, and 24 h. Falling gray lines in Fig. 7e represent the quenching of PL intensity between the reaction progress subjected to solvent evaporation, thereby increasing the concentration. The PL intensities of concentrated sample reaction time intervals are at 0.5 h, 1.5 h, 2.5 h, 3.5 h, 6.5 h, and 24.5 h. We expect that at the increased concentrations, the stoichiometry of NCs could be altered as a result of changes in the local concentration of Cs$^+$ due to the disturbance to ligand dynamics associated with modified electrostatic interactions.

The PL emission of the sample is quenched at the concentrated condition after hexane evaporation, whereas upon re-dilution, it regains its PL emission. Blue dots imply PL emission at regular dilutions, and grey ones indicate the concentrated conditions. This procedure was repeated several times in a period of over 24 hours, and the results of cyclic quenching and recovery of PL emission are presented in Fig. 7e. As a control experiment, samples without hexane solvent and with hexane undisturbed were prepared, and their PL intensity was measured at the same time intervals. The results are compared in Fig. S30–S33,† and show that there is no or ill-defined reaction (no signs of CsPbBr$_3$ NBs) for the sample without hexane. The undisturbed reaction shows a gradual PL emission but a relatively lower intensity than that in the cyclic experiment. Interestingly, based on the PL emission results of the cyclic experiment, the reaction "remembers" the original reaction path with a quicker resurgence of NB formation at every dilution step. In addition, kinetically stable products trapped at suitable dilution predominated over spontaneous aggregation directed by stoichiometry. Our results on the study of the effect of concentration align with the findings that dilution is the prerequisite to producing luminescent nanobelts. Some of the recently reported NB syntheses are two-step processes, where, at first, the formation of non-luminescence nanostructures occurs. Next, in the second step, the redissolution of non-luminescence species in a solvent to the desired dilution results in the formation of nanobelts. From our experiment, one can conclude that the reaction can be controlled *via* suitable concentrations (a direct synthetic protocol) without any need for stepwise synthesis or post-synthetic purifications.[32]
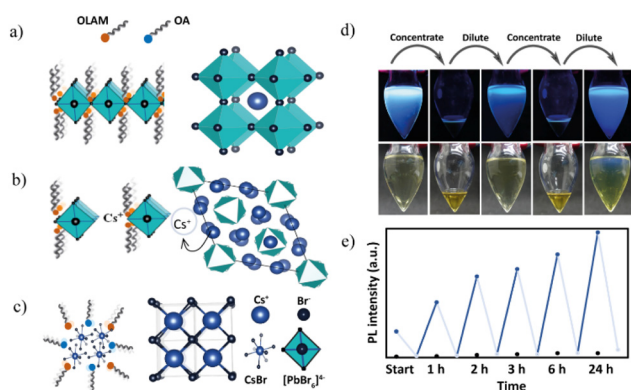

Fig. 7 (a–c) Schematic representation of the effect of stoichiometry on the final crystal structures. At δ_1, the attachment of (PbBr$_6$)$^-$ octahedra predominantly occurs; at δ_2, the Cs$_4$PbBr$_6$ structure where the octahedra are separated by the Cs$^+$ ions is predominant; at δ_3, the structures are influenced by Cs$^+$ and Br$^-$, and, as a result, the final products are CsBr structures. (d) Photographs of the solutions (NBs) for the cyclic experiment in visible (bottom) and UV light (top) and (e) the corresponding PL experiment. The black dots represent a control experiment having two precursors (without hexane solvent).

Finally, to study the effect of polarity on the reaction process, first, we studied the effect of aging of CsPbBr$_3$ NB phase without quenching it by subjection to washing procedures. Fig. 8a highlights that continuing the reaction for 24 hours has a dramatic impact on PL intensity and peak position as the emission grows strongly and exhibits a uniform redshift from 420 nm to 465 nm over time. This redshift reflects the NB diameter associated with quantum confinement. Moreover, these reactions could be stopped at any time by the addition of antisolvent, *e.g.*, methyl acetate. The PL results are in good agreement with the TEM observations, which confirm the growth of ultrathin nanobelts (~3 nm) to NBs (~6 nm) to thicker NBs (~9 nm), as can be seen from Fig. 8b–e. The formation of nanobelts is quite spontaneous, so the provided precursors were immediately consumed, leading to the formation of the ultrathin NBs. Therefore, we assume that the formation of thicker NBs occurred through the fusing mechanism given in Fig. 8e. Importantly, in our experimental conditions, either side of excess host **P$_{Pb-br}$** or titrant **P$_{Cs-ol}$**, could not produce cube-shaped CsPbBr$_3$ NCs. Few reports show the formation of such CsPbBr$_3$ NCs at RT using ligands other than OA and OLAM,[16,44] wherein the ligands themselves provide sufficient polar and acidic strength to change the dynamics toward the different sizes and morphologies. Since such conditions were not provided in our reaction system, there is less likelihood of the formation of CsPbBr$_3$ nanocubes. To prove the same, we performed experiments with the addition of ethanol (a polar solvent), and, as expected, we observed the formation of cubic CsPbBr$_3$ instantaneously (Fig. S34†). As prepared highly emissive CsPbBr$_3$ was stable after washing with methyl acetate, centrifuging, and redispersing the pellet in hexane. The addition of microliter quantities of ethanol to the $\delta = 1 : 0.25$ conditions leads to a redshift of the PL positions with respective quantum-confined nanostructures. The shift is higher (100 nm) at higher amounts of ethanol and lower (30 nm) at 5 µL of ethanol in comparison to that of the nanobelts formed in the absence of polar reagents. Fig. 8f shows photographs of such quantum-confined species and their respective PL emissions. This can be explained that ethanol does not allow sufficient passivation of ligands on the nanobelts' surface; they tend to grow upon oriented self-assembly to next-level quantum confined structures (Fig. 8g). The thermal and polar influences could aid ligand-destabilization-induced crystallization for the formation of CsPbBr$_3$ NCs.[45] These observations can also support the formation of other nanostructures in a solution depending on the polar medium's strength and amount. The growth kinetics of the reaction is highly influenced by the polarity of the solvent, which could significantly alter the reaction pathway.

Conclusions

In summary, we have demonstrated the growth kinetics of transformations throughout the reaction path of anionic [PbBr$_x$]$^{n-}$ crystallization with Cs$^+$ as governed by the supply of Cs$^+$ to offer a landscape for diverse cesium–(lead)–bromide NCs at RT in a non-polar solvent. In the process, we provide new insights into the transformation of the crystalline phase and the habit of kinetically stable states. By increasing the Cs$^+$ concentration with respect to PbBr$_2$, we observed the formation of CsPbBr$_3$ NBs with uniform diameters and thickness (δ_1), followed by larger rhombohedral and spherical Cs$_4$PbBr$_6$ (δ_2), and finally spherical and cubic CsBr NCs (δ_3). This study offers possible reasons behind the size and shape control of kinetically stable phases at suitable concentrations and packing patterns of the self-assembled states, for example, the CsPbBr$_3$ nanobelt scission to nanoplatelets, size variation in Cs$_4$PbBr$_6$ NCs, and effect of polarity, dilution, *etc*. Depending on the crystal nature, they can form large HCP and CCP self-assembled monolayers on solid surfaces, even from the stage of NC seeds. Additionally, this facile method for self-pattern assemblies from these as-synthesized NCs could contribute to the application of single and binary NC superlattices for super-fluorescence. This study highlights that the precise size control of NCs is possible and indeed related to the availability of Cs$^+$ and its dynamic exchange to mediate or guide the crystal habit and growth kinetics. Overall, our findings highlight the concepts of rapid crystallization, shifting the equilibrium to a designated path by chemical input as an internal cue (an unprecedented approach for Cs–Pb–Br metathesis reaction at room temperature) and ultimately controlling the growth kinetics of the perovskite NC systems.
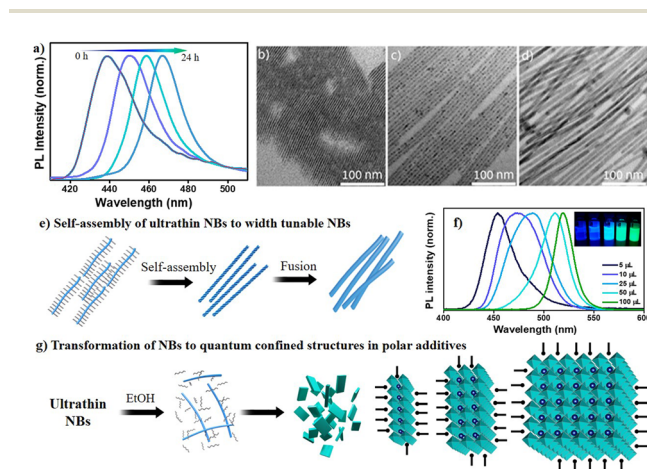

Fig. 8 (a) PL emission of ultrathin NBs upon the continuation of reaction for several hours; corresponding TEM images are presented in (b) to (d). (e) Schematic illustration of the RT growth profile of NBs from lamellar-type Cs−Pb−Br structures to 9 nm NBs. (f) PL emission of ethanol-induced growth of NBs to NCs and corresponding photographs under UV light. (g) Schematic illustration of the transformation of NBs in the presence of ethanol resulting in ligand destabilization on the NB surface and followed by proactive growth.

Author contributions

UT conceived the project. UT, MP, and AKB designed the experiments. MP, ZG, and YW performed the experiments. MP,

UT, and AKB analyzed the data. AKB and UT co-wrote the manuscript and all the authors approved the manuscript. MP and ZG contributed equally.

Conflicts of interest

The authors declare no competing financial interests.

Acknowledgements

References

1 Q. A. Akkerman, G. Rainò, M. V. Kovalenko and L. Manna, *Nat. Mater.*, 2018, **17**, 394–405.

2 Y. Xia, Y. Xiong, B. Lim and S. E. Skrabalak, *Angew. Chem., Int. Ed.*, 2009, **48**, 60–103.

3 F. Wang, V. N. Richards, S. P. Shields and W. E. Buhro, *Chem. Mater.*, 2014, **26**, 5–21.

4 L. Protesescu, S. Yakunin, M. I. Bodnarchuk, F. Krieg, R. Caputo, C. H. Hendon, R. X. Yang, A. Walsh and M. V. Kovalenko, *Nano Lett.*, 2015, **15**, 3692–3696.

5 J. Shamsi, A. S. Urban, M. Imran, L. De Trizio and L. Manna, *Chem. Rev.*, 2019, **119**, 3296–3348.

6 G. Nedelcu, L. Protesescu, S. Yakunin, M. I. Bodnarchuk, M. J. Grotevent and M. V. Kovalenko, *Nano Lett.*, 2015, **15**, 5635–5640.

7 G. Almeida, L. Goldoni, Q. Akkerman, Z. Dang, A. H. Khan, S. Marras, I. Moreels and L. Manna, *ACS Nano*, 2018, **12**, 1704–1711.

8 S. Toso, D. Baranov and L. Manna, *ACS Energy Lett.*, 2020, **5**, 3409–3414.

9 S. Bera, R. K. Behera, S. D. Adhikari, A. K. Guria and N. Pradhan, *J. Phys. Chem. Lett.*, 2021, **12**, 11824–11833.

10 L. Wu, H. Hu, Y. Xu, S. Jiang, M. Chen, Q. Zhong, D. Yang, Q. Liu, Y. Zhao, B. Sun, Q. Zhang and Y. Yin, *Nano Lett.*, 2017, **17**, 5799–5804.

11 F. Palazon, C. Urso, L. De Trizio, Q. Akkerman, S. Marras, F. Locardi, I. Nelli, M. Ferretti, M. Prato and L. Manna, *ACS Energy Lett.*, 2017, **2**, 2445–2448.

12 J.-R. Wen, B. J. Roman, F. A. Rodriguez Ortiz, N. Mireles Villegas, N. Porcellino and M. Sheldon, *Chem. Mater.*, 2019, **31**, 8551–8557.

13 J. Shamsi, Z. Dang, P. Ijaz, A. L. Abdelhady, G. Bertoni, I. Moreels and L. Manna, *Chem. Mater.*, 2018, **30**, 79–83.

14 T. Udayabhaskararao, L. Houben, H. Cohen, M. Menahem, I. Pinkas, L. Avram, T. Wolf, A. Teitelboim, M. Leskes, O. Yaffe, D. Oron and M. Kazes, *Chem. Mater.*, 2018, **30**, 84–93.

15 S. K. Balakrishnan and P. V. Kamat, *Chem. Mater.*, 2018, **30**, 74–78.

16 A. Pan, B. He, X. Fan, Z. Liu, J. J. Urban, A. P. Alivisatos, L. He and Y. Liu, *ACS Nano*, 2016, **10**, 7943–7954.

17 S. Sun, D. Yuan, Y. Xu, A. Wang and Z. Deng, *ACS Nano*, 2016, **10**, 3648–3657.

18 B. A. Koscher, Z. Nett and A. P. Alivisatos, *ACS Nano*, 2019, **13**, 11825–11833.

19 S. Bera, R. K. Behera and N. Pradhan, *J. Am. Chem. Soc.*, 2020, **142**, 20865–20874.

20 C. Otero-Martínez, D. García-Lojo, I. Pastoriza-Santos, J. Pérez-Juste and L. Polavarapu, *Angew. Chem., Int. Ed.*, 2021, **60**, 26677–26684.

21 Q. A. Akkerman, S. G. Motti, A. R. Srimath Kandada, E. Mosconi, V. D'Innocenzo, G. Bertoni, S. Marras, B. A. Kamino, L. Miranda, F. De Angelis, A. Petrozza, M. Prato and L. Manna, *J. Am. Chem. Soc.*, 2016, **138**, 1010–1016.

22 L. Peng, A. Dutta, R. Xie, W. Yang and N. Pradhan, *ACS Energy Lett.*, 2018, **3**, 2014–2020.

23 Y. Wang, H. Zhao, M. Piotrowski, X. Han, Z. Ge, L. Dong, C. Wang, S. K. Pinisetty, P. K. Balguri, A. K. Bandela and U. Thumu, *Micromachines*, 2022, **13**, 1318.

24 J. C. Dahl, X. Wang, X. Huang, E. M. Chan and A. P. Alivisatos, *J. Am. Chem. Soc.*, 2020, **142**, 11915–11926.

25 H. Huang, Y. Li, Y. Tong, E.-P. Yao, M. W. Feil, A. F. Richter, M. Döblinger, A. L. Rogach, J. Feldmann and L. Polavarapu, *Angew. Chem., Int. Ed.*, 2019, **58**, 16558–16562.

26 F. Zhang, H. Zhong, C. Chen, X.-g. Wu, X. Hu, H. Huang, J. Han, B. Zou and Y. Dong, *ACS Nano*, 2015, **9**, 4533–4542.

27 Y. Dong, T. Qiao, D. Kim, D. Parobek, D. Rossi and D. H. Son, *Nano Lett.*, 2018, **18**, 3716–3722.

28 H. Yang, Y. Zhang, J. Pan, J. Yin, O. M. Bakr and O. F. Mohammed, *Chem. Mater.*, 2017, **29**, 8978–8982.

29 A. A. M. Brown, P. Vashishtha, T. J. N. Hooper, Y. F. Ng, G. V. Nutan, Y. Fang, D. Giovanni, J. N. Tey, L. Jiang, B. Damodaran, T. C. Sum, S. H. Pu, S. G. Mhaisalkar and N. Mathews, *Chem. Mater.*, 2021, **33**, 2387–2397.

30 C. Otero-Martínez, J. Ye, J. Sung, I. Pastoriza-Santos, J. Pérez-Juste, Z. Xia, A. Rao, R. L. Z. Hoye and L. Polavarapu, *Adv. Mater.*, 2022, **34**, 2107105.

31 X. Li, Y. Wu, S. Zhang, B. Cai, Y. Gu, J. Song and H. Zeng, *Adv. Funct. Mater.*, 2016, **26**, 2435–2445.

32 Y. Xu, Q. Zhang, L. Lv, W. Han, G. Wu, D. Yang and A. Dong, *Nanoscale*, 2017, **9**, 17248–17253.

33 Y. Liu, M. Guo, S. Dong, X. Jiao, T. Wang and D. Chen, *J. Mater. Chem. C*, 2018, **6**, 7797–7802.

34 A. Kostopoulou, M. Sygletou, K. Brintakis, A. Lappas and E. Stratakis, *Nanoscale*, 2017, **9**, 18202–18207.

35 E. H. Massasa, R. Strassberg, A. Vurgaft, Y. Kauffmann, N. Cohen and Y. Bekenstein, *Nano Lett.*, 2021, **21**, 5564–5571.

36 M. C. Weidman, M. Seitz, S. D. Stranks and W. A. Tisdale, *ACS Nano*, 2016, **10**, 7830–7839.

37 Z. Liu, Y. Bekenstein, X. Ye, S. C. Nguyen, J. Swabeck, D. Zhang, S.-T. Lee, P. Yang, W. Ma and A. P. Alivisatos, *J. Am. Chem. Soc.*, 2017, **139**, 5309–5312.

38 Q. A. Akkerman, S. Park, E. Radicchi, F. Nunzi, E. Mosconi, F. De Angelis, R. Brescia, P. Rastogi, M. Prato and L. Manna, *Nano Lett.*, 2017, **17**, 1924–1930.

39 Y. Yang, J. T. Lee, T. Liyanage and R. Sardar, *J. Am. Chem. Soc.*, 2019, **141**, 1526–1536.

40 A. Pan, M. Jurow, Y. Zhao, F. Qiu, Y. Liu, J. Yang, J. J. Urban, L. He and Y. Liu, *Nanoscale*, 2017, **9**, 17688–17693.

41 J. Hui, Y. Jiang, Ö. Ö. Gökçinar, J. Tang, Q. Yu, M. Zhang and K. Yu, *Chem. Mater.*, 2020, **32**, 4574–4583.

42 I. Cherniukh, G. Rainò, T. Stöferle, M. Burian, A. Travesset, D. Naumenko, H. Amenitsch, R. Erni, R. F. Mahrt, M. I. Bodnarchuk and M. V. Kovalenko, *Nature*, 2021, **593**, 535–542.

43 B. Hudait, S. K. Dutta and N. Pradhan, *ACS Energy Lett.*, 2020, **5**, 650–656.

44 J. Zhao, S. Cao, Z. Li and N. Ma, *Chem. Mater.*, 2018, **30**, 6737–6743.

45 B. J. Bohn, Y. Tong, M. Gramlich, M. L. Lai, M. Döblinger, K. Wang, R. L. Z. Hoye, P. Müller-Buschbaum, S. D. Stranks, A. S. Urban, L. Polavarapu and J. Feldmann, *Nano Lett.*, 2018, **18**, 5231–5238.